CAN NEUTRINO-COOLED ACCRETION DISKS BE AN ORIGIN OF GAMMA-RAY BURSTS?

KAZUNORI KOHRI AND SHIN MINESHIGE
Yukawa Institute for Theoretical Physics, Kyoto University, Kyoto 606-8502, Japan;
kohri@yukawa.kyoto-u.ac.jp, minesige@yukawa.kyoto-u.ac.jp

ABSTRACT

It is often proposed that a massive torus with approximately solar mass surrounding a stellar-mass black hole could be a central engine of gamma-ray bursts. We study the properties of such massive accretion tori (or disks) based on the α viscosity model. For surface density exceeding about 10^{20} g cm^{-2}, which is realized when $\sim 1 \ M_\odot$ of material is contained within a disk of size $\sim 5 \times 10^6$ cm, we find that (1) the luminosity of photons is practically zero because of significant photon trapping, (2) neutrino cooling dominates over advective cooling, (3) the pressure of degenerate electrons dominates over the pressure of gas and photons, and (4) the magnetic field strength exceeds the critical value of about 4×10^{13} G, even if we take 0.1% of the equipartition value. The possible observable quantum electrodynamical (QED) effects arising from supercritical fields are discussed. Most interestingly, photon splitting may occur, producing a significant number of photons of energies below ~ 511 keV, thereby possibly suppressing $e^\pm$ pair creation.

Subject headings: accretion, accretion disks — black hole physics — gamma rays: bursts — neutrinos

1. INTRODUCTION

Research on gamma-ray bursts (GRBs) has made rapid progress over the past decade, particularly after the discovery of afterglows by *BeppoSAX* (see recent reviews by Mészáros, Rees, & Wijers 1999; Piran 2000; Mészáros 2001). The current common belief is that GRBs are the most energetic explosions that ever occurred in the universe, releasing energies of $\sim 10^{51}$–10^{53} ergs in only a few to few tens of seconds. It is also widely argued that GRBs result from the conversion of the kinetic energy of ultrarelativistic particles created within a fireball. A relativistic fireball shock model was proposed to resolve the compactness problem and has had some success in explaining how the GRB and afterglow radiation arise (Rees & Mészáros 1992, 1994; Wijers & Galama 1999).

However, the central engines of GRBs creating initial hot plasma or extremely energetic particles are not well understood yet, mainly because of the fact that they are hidden from our view. It is usually argued that relativistic phenomena should be somehow involved, since otherwise it is difficult to explain huge fluence and rapid burstlike bust profiles. (Narayan, Paczyński, & Piran 1992). Along this line, many interesting possibilities have been proposed so far, such as (1) mergers of double neutron star (NS) binaries or NSs and black holes (BHs) (Paczyński 1986, 1991; Goodman 1986; Eichler et al. 1989); (2) BH-WD (white dwarf) mergers (Fryer et al. 1999); (3) BH–helium star mergers (Fryer et al. 1999); (4) failed supernovae (or collapsars, Woosley 1993; Paczyński 1998; MacFadyen & Woosley 1999); and (5) magnetars, rapidly spinning neutron stars with extremely large magnetic fields (Usov 1992, 1994; Thompson 1994; Spruit 1999). It is of great importance to note that almost all the models (except for the magnetar hypothesis) predict a similar configuration as an end result, namely, the formation of a few solar mass black hole surrounded by a temporary debris torus (or disk) with mass of 0.01–1.0 $M_\odot$, whose accretion can provide a sudden release of gravitational energy (Mészáros et al. 1999). Then the key issue will be to understand the properties of such a compact and massive disk associated with a huge mass accretion rate.

Accretion models for gamma-ray bursts were first considered by Narayan et al. (1992), and have recently been discussed in more detail by Popham, Woosley, & Fryer (1999) and Narayan, Piran, & Kumar (2001, hereafter NPK01). According to them, neutrino cooling dominates over radiative loss at very huge accretion rates (see, however, Chevalier 1996; see also Ruffert & Janka 1999 for a numerical simulation of a binary merger including neutrino losses). Therefore, such disks (or flows) are called "neutrino-dominated accretion flows" (NDAFs). In the present study, we elucidate the theory of NDAFs based on the α viscosity prescription, paying special attention to their thermal structure and the implications of the expected huge magnetic fields. We present the resulting equilibrium solutions and properties of neutrino-cooled disks in § 2. We then discuss the effects of huge magnetic fields and the implications for neutrino emission in § 3. Conclusions are presented in § 4.

2. STRUCTURE OF NEUTRINO-COOLED DISK

2.1. Σ-*T Diagram*

In this study we adopt the following basic equations based on Newtonian dynamics, for simplicity (see, e.g., Kato, Fukue, & Mineshige 1998). We use the cylindrical coordinates (r, φ, z). Then the mass conservation in the vertical and radial directions, respectively, is represented by

$$\rho = \frac{\Sigma}{2H} \quad \text{and} \quad \dot{M} = -2\pi r v_r \Sigma \ , \tag{1}$$

where ρ is the matter density, Σ is the surface density of the disk, H is the disk half-thickness, $\dot{M}$ is the mass accretion rate, and v_r is the radial velocity (negative for inflow). The disk half-thickness is given by, from hydrostatic balance in the vertical direction,

$$H = c_s/\Omega \ , \tag{2}$$

where the (isothermal) sound velocity c_s is defined by

$$c_s \equiv \sqrt{p/\rho} \, , \tag{3}$$

with the pressure p. The angular velocity, Ω, is in the Newtonian approximation given by

$$\Omega = \sqrt{GM_{\mathrm{BH}}/r^3} \, , \tag{4}$$

where G is the gravitational constant, and M_{BH} is the black hole mass. The pressure is composed of three terms:

$$p = p_{\mathrm{rad}} + p_{\mathrm{gas}} + p_d \, , \tag{5}$$

where p_{rad} is the radiation pressure, p_{gas} is the gas pressure of the nonrelativistic and nondegenerate particles, and p_d is the pressure of the degenerate particles. The radiation pressure is

$$p_{\mathrm{rad}} = \frac{a}{6} g_* T^4 \, , \tag{6}$$

where g_* is statistical degree of freedom in the radiation ($=2$ for γ, or $11/2$ for γ and $e^+ e^-$ plasma), and a is the radiation constant. The gas pressure is

$$p_{\mathrm{gas}} = \sum_i n_i k_{\mathrm{B}} T \, , \tag{7}$$

where k_{B} is the Boltzmann constant, n_i is the number density of particle i, and the suffix i runs the nonrelativistic and nondegenerate particles at the temperature (e.g., e^- and nucleons at $T \lesssim m_e c^2/k_{\mathrm{B}}$). The pressure of the degenerate particles is written as

$$p_d = p_{d,\mathrm{nonrel}} + p_{d,\mathrm{rel}} \cdot \tag{8}$$

Then

$$p_{d,\mathrm{nonrel}} = \sum_{i=\mathrm{nonrel}} \frac{1}{5} \left(\frac{6\pi^2}{g_i} \right)^{2/3} \frac{\hbar^2 n_i^{5/3}}{m_i} \, , \tag{9}$$

for nonrelativistic particles that satisfy the condition of the degeneracy

$$n_i \gg g_i (m_i k_{\mathrm{B}} T/2\pi \hbar^2)^{3/2} \, , \tag{10}$$

for $T \ll m_i c^2/k_{\mathrm{B}}$ and $\mu_i \ll m_i c^2$, with mass m_i, statistical degree of freedom g_i, and chemical potential μ_i; and

$$p_{d,\mathrm{rel}} = \sum_{i=\mathrm{rel}} \frac{1}{4} \left(\frac{6\pi^2}{g_i} \right)^{1/3} \hbar^2 c n_i^{4/3} \, , \tag{11}$$

for relativistic particles that satisfy the condition of the degeneracy

$$n_i \gg g_i (k_{\mathrm{B}} T/\hbar c)^3 / \pi^2 \, , \tag{12}$$

for $T \gg m_i c^2/k_{\mathrm{B}}$ or $\mu_i \gg m_i c^2$. In this study, for simplicity we assume complete degeneracy whenever the above condition of degeneracy is satisfied.

In Figure 1, we plot the contours of the matter density on the (Σ, T) plane. From this figure we can read off the matter density. It also discriminates the regions in which each pressure component is dominant and also the regions in which electrons and/or nucleons are degenerate. We understand that degeneracy pressure is important at high-density and

low-temperature regimes. Such regimes inevitably appear in very massive disks, and one can never neglect the contributions of degeneracy pressure in GRBs, unlike the cases of binary systems or galactic centers. We also note that one should distinguish the regime in which only electrons are degenerate from the one in which both electrons and nucleons are degenerate.

2.2. *Chemical Potential of Electrons*

When electrons are degenerate, there emerges an important consequence for the process of neutrino emission, i.e., since the pair creation of electrons and positrons in the electromagnetic thermal bath is suppressed by the charge neutrality (see below), the neutrino emission is also suppressed. (This is not discussed in NPK01.) The electron chemical potential μ_e is determined by the condition of charge neutrality,

$$n_p = n_{e^-} - n_{e^+}, \tag{13}$$

with the number density of electrons and positrons

$$n_{e^-} = \frac{1}{\hbar^3 \pi^2} \int_0^\infty dp\, p^2 \frac{1}{\exp\left[\left(\sqrt{p^2 c^2 + m_e^2 c^4} - \mu_e \right)/k_{\mathrm{B}} T \right] + 1} \, , \tag{14}$$

$$n_{e^+} = \frac{1}{\hbar^3 \pi^2} \int_0^\infty dp\, p^2 \frac{1}{\exp\left[\left(\sqrt{p^2 c^2 + m_e^2 c^4} + \mu_e \right)/k_{\mathrm{B}} T \right] + 1} \cdot \tag{15}$$

In the following sections, it is convenient to introduce a dimensionless chemical potential for electrons, which is defined by

$$\eta_e = \mu_e / k_{\mathrm{B}} T \, . \tag{16}$$

Then, the complete degeneracy of electrons corresponds to $\eta_e \gg 1$, and the charge neutrality in equation (13) becomes

$$n_p \simeq n_{e^-} \simeq \frac{1}{3\pi^2} \left(\frac{\mu_e}{\hbar c} \right)^3 . \tag{17}$$

The chemical potentials of protons and neutrons are defined through the relation

$$n_p = \frac{1}{\hbar^3 \pi^2} \int_0^\infty dp\, p^2 \frac{1}{\exp\left[\left(\sqrt{p^2 c^2 + m_p^2 c^4} - \mu_p \right)/k_{\mathrm{B}} T \right] + 1} \, , \tag{18}$$

$$n_n = \frac{1}{\hbar^3 \pi^2} \int_0^\infty dp\, p^2 \frac{1}{\exp\left[\left(\sqrt{p^2 c^2 + m_n^2 c^4} - \mu_n \right)/k_{\mathrm{B}} T \right] + 1} \cdot \tag{19}$$

If the nucleons are not degenerate, we have

$$n_i = 2 \left(\frac{m_i k_{\mathrm{B}} T}{2\pi \hbar^2} \right)^{3/2} \exp\left[-\frac{(m_i c^2 - \mu_i)}{k_{\mathrm{B}} T} \right] \tag{20}$$

for $i = p$ and n. On the other hand, if nucleons are degenerate, we have

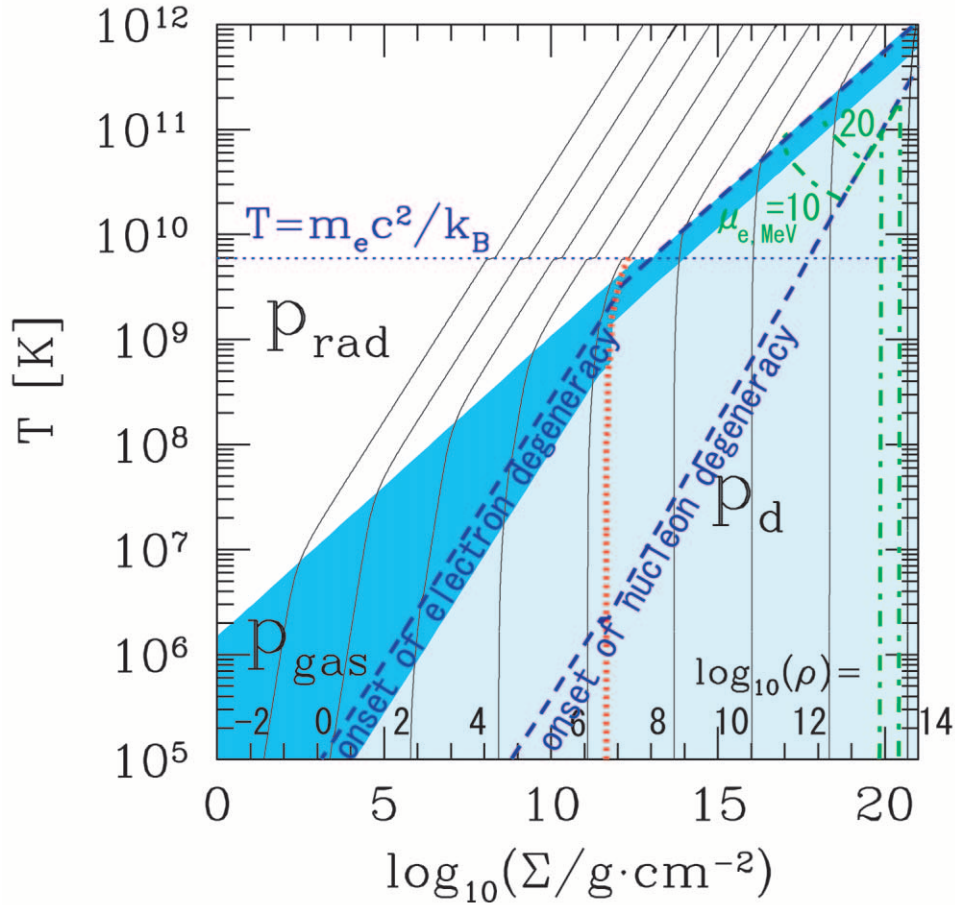$$n_i = \frac{1}{3\pi^2} \left(\frac{2\tilde{\mu}_i m_i}{\hbar^2} \right)^{3/2} \tag{21}$$

Fig. 1.—Contours of the matter density on the (Σ, T) plane for the case in which the black hole mass is $M_{BH} = 3 \ M_\odot$ and $r = 4r_S$, where r_S is the Schwarzschild radius. The solid lines denote the contours of the matter density for $\log(\rho/\text{g cm}^{-3}) = -2, 0, 2, \ldots, 14$. The dark (or light) shadowed region shows where p_{gas} (p_d) dominantly contributes to the total pressure, while the white region shows where p_{rad} is dominant. The left and right thick dashed lines denote the loci where electron and nucleon degeneracy, respectively, begin to take place. Namely, electrons (or nucleons) are degenerate because of higher density on the right side of the left (right) dashed line. The horizontal dotted line shows the temperature corresponding to the electron mass m_e. The thick dotted line shows the boundary where electrons become relativistic as a result of higher energy density ($\rho \gtrsim 2 \times 10^6 \text{g cm}^{-3}$) while $T \lesssim m_e c^2/k_B$. The dot-dashed lines represent the chemical potential of electrons in units of MeV, $\mu_{e,\text{MeV}} = 10$ and 20, from the lower left to the upper right.

for the complete degenerate limit with

$$\tilde{\mu}_i = \mu_i - m_i c^2 . \tag{22}$$

In this study, we did not directly solve the exact equation (13) to derive the chemical potential of electrons. Instead, we performed the following approximated computations in the complete degeneracy regime ($\eta_e \gg 1$). As will be shown later, nucleons are in β-equilibrium at a high temperature, $T \gtrsim 5.0 \times 10^{10} \text{ K}(\alpha/0.1)^{1/5}(r/4r_S)^{-3/10}(M_{BH}/3 \ M_\odot)^{-1/5}$, where the neutrino emissions are effective and mainly contribute to the cooling process. Then the chemical equilibrium is realized,

$$\mu_p + \mu_e = \mu_n , \tag{23}$$

or

$$\tilde{\mu}_p + \mu_e - Q = \tilde{\mu}_n , \tag{24}$$

where $Q = (m_n - m_p)c^2 \simeq 1.29$ MeV. In the regime where only electrons are degenerate, β-equilibrium means

$$\frac{n_p}{n_n} = \exp\left[\frac{(Q - \mu_e)}{(k_B T)}\right] . \tag{25}$$

The electron fraction $Y_e \equiv n_p/(n_p + n_n)$ is related to the above ratio by $Y_e = 1/[1 + (n_p/n_n)^{-1}]$. Combined with the condition of the charge neutrality, i.e., equation (17), we may only solve the equation

$$\frac{\rho}{m_p}\exp\left(-\frac{\mu_e}{k_B T}\right) = \frac{1}{3\pi^2}\left(\frac{\mu_e}{\hbar c}\right)^3 \tag{26}$$

for $\mu_e \gg k_B T \gg Q$. On the other hand, it is relatively easy for us to calculate μ_e in the regime where both electrons and nucleons are degenerate. From the charge neutrality (eq. [17]) and chemical equilibrium (eq. [24]), we find that $\mu_e \sim \tilde{\mu}_n \gg \tilde{\mu}_p$ for $k_B T \ll \mu_e < O(10^2)$ MeV. Then, from equation (21) we can approximately estimate the chemical potential of electrons as

$$\mu_e \simeq \tilde{\mu}_n \tag{27}$$

$$\simeq 6.628 \text{ MeV } (\rho/10^{13}\text{g cm}^{-3})^{2/3} , \tag{28}$$

in the complete-degeneracy limit of both electrons and nucleons.

We also plot the contours of the chemical potential of electrons in units of MeV ($\mu_{e,\text{MeV}} = 10$ and 20) in Figure 1. The chemical potential of electrons play important roles in

estimating the emission rates of neutrinos, which will be discussed in the next subsection.

2.3. *Heating and Cooling Rates*

The most important relation in the accretion disk theory is the energy balance between the heating and cooling processes. Distinct branches (such as a standard disk or a slim disk, etc.) appear because of different heating and/or cooling sources being dominant. According to the standard α viscosity model, we express the vertically integrated heating rate (over a half-thickness, H) as

$$Q^+ = Q^+_{\mathrm{vis}} = \tfrac{9}{8}\nu\Sigma\Omega^2 , \qquad (29)$$

where Q^+_{vis} denotes the viscous heating rate per unit surface area, and the kinetic viscosity ν is related to the viscosity parameter α by

$$\nu = \tfrac{2}{3}\alpha c_s H . \qquad (30)$$

If we assume angular momentum conservation, we obtain

$$\nu\Sigma = \frac{\dot{M}}{3\pi}\left(1 - \sqrt{\frac{r_{\mathrm{in}}}{r}}\right) , \qquad (31)$$

where r_{in} is the radius of the inner edge of the disk ($= 3r_{\mathrm{S}}$). From equations (29), (30), and (31), we can relate the heating rate to the mass accretion rate,

$$\dot{M} = \frac{8\pi}{3}\Omega^{-2}\left(1 - \sqrt{\frac{r_{\mathrm{in}}}{r}}\right)^{-1}Q^+ . \qquad (32)$$

The cooling rate is, on the other hand, a summation of three major contributions,

$$Q^- = Q^-_{\mathrm{rad}} + Q^-_{\mathrm{adv}} + Q^-_\nu , \qquad (33)$$

where Q^-_{rad} is the radiative cooling rate, Q^-_{adv} is the advective energy transport (Abramowicz et al. 1988), and Q^-_ν is the cooling rate due to neutrino loss. Note that instead of including advective energy transport in the energy equation, NPK01 adopted the view of CDAF (convection-dominated accretion flow; Igumenshchev, Abramowicz, & Narayan 2000, Narayan, Igumenshchev, & Abramowicz 2000; Quataert & Gruzinov 2000). In the present study, we retain the classical picture based on the (vertical) one-zone treatment (e.g., Kato et al. 1998), since it is not yet clear whether CDAF provides a precise description of the flow structure not only in the low-luminosity regimes but also in the hyperaccretion regimes. However, such a distinction is not essential here, since we are concerned with the regimes of even higher accretion rates, in which neutrino emission is substantial (as discussed below).

The radiative cooling rate is

$$Q^-_{\mathrm{rad}} = \frac{g_*\sigma_s T^4}{2\tau_{\mathrm{tot}}} , \qquad (34)$$

where $\sigma_s = \pi^2 k_{\mathrm{B}}^4/(60\hbar^3 c^2)$ is the Stefan-Boltzmann constant, and the optical depth, τ_{tot}, is given by

$$\tau_{\mathrm{tot}} = \kappa_{\mathrm{R}}\rho H = \frac{\kappa_{\mathrm{R}}\Sigma}{2} , \qquad (35)$$

with κ_{R} being the Rosseland mean opacity,

$$\kappa_{\mathrm{R}} = 0.40 + 0.64 \times 10^{23}\left(\frac{\rho}{\mathrm{g\ cm^{-3}}}\right)\left(\frac{T}{\mathrm{K}}\right)^{-3}\mathrm{g^{-1}\ cm^2} . \qquad (36)$$

The advective cooling rate is given by (Kato et al. 1998)

$$Q^-_{\mathrm{adv}} = \Sigma T v_r \frac{ds}{dr} , \qquad (37)$$

where the radial velocity is $v_r = -\dot{M}/(2\pi r\Sigma)$, and s denotes the entropy per particle,

$$s = (s_{\mathrm{rad}} + s_{\mathrm{gas}})/\rho . \qquad (38)$$

Here, the entropy density of the radiation is

$$s_{\mathrm{rad}} = \tfrac{2}{3}ag_* T^3 , \qquad (39)$$

and the entropy density of the gas (i.e., nonrelativistic particles) is

$$s_{\mathrm{gas}} = \sum_i n_i\left\{\frac{5}{2} + \ln\left[\frac{g_i}{n_i}\left(\frac{m_i T}{2\pi}\right)^{3/2}\right]\right\} , \qquad (40)$$

where the suffix i runs over nonrelativistic nucleons and electrons, and g_i is the statistical degree of freedom of the particle. In the following, we approximated ds/dr as s/r. Note that since the entropy of degenerate particles is small in the complete-degeneracy limit, we neglect it here.

The neutrino cooling rate is composed of four terms:

$$Q^-_\nu = (\dot{q}_{Ne} + \dot{q}_{e^+e^-} + \dot{q}_{\mathrm{brems}} + \dot{q}_{\mathrm{plasmon}})H, \qquad (41)$$

where $\dot{q}_{Ne}$ is the electron-positron capture rate by a nucleon N, $\dot{q}_{e^+e^-}$ is the electron-positron pair annihilation rate, $\dot{q}_{\mathrm{brems}}$ is the nucleon-nucleon bremsstrahlung rate, and $\dot{q}_{\mathrm{plasmon}}$ is the rate of plasmon decays. Note that NPK01 considered only the case of nondegenerate electrons in first two terms on the right-hand side of equation (41). However, the case of degenerate electrons in the first two terms and the other two terms could be also important.

The electron-positron capture rate is represented by two terms:

$$\dot{q}_{Ne} = \dot{q}_{p+e^-\to n+\nu_e} + \dot{q}_{n+e^+\to p+\bar{\nu}_e} , \qquad (42)$$

with

$$\dot{q}_{p+e^-\to n+\nu_e} = \frac{G_{\mathrm{F}}^2}{2\pi^3\hbar^3 c^2}(1 + 3g_A)n_p$$
$$\times \int_Q^\infty dE_e\, E_e\sqrt{E_e^2 - m_e^2 c^4}(E_e - Q)^3$$
$$\times \frac{1}{\exp[(E_e - \mu_e)/k_{\mathrm{B}}T] + 1} , \qquad (43)$$

$$\dot{q}_{n+e^+\to p+\bar{\nu}_e} = \frac{G_{\mathrm{F}}^2}{2\pi^3\hbar^3 c^2}(1 + 3g_A)n_n$$
$$\times \int_{m_e c^2}^\infty dE_e\, E_e\sqrt{E_e^2 - m_e^2 c^4}(E_e + Q)^3$$
$$\times \frac{1}{\exp[(E_e + \mu_e)/k_{\mathrm{B}}T] + 1} , \qquad (44)$$

where G_{F} is the Fermi coupling constant ($= 2.302 \times$

10^{-22} cm MeV^{-1}), and g_A is the axial-vector coupling constant of a nucleon (~ 1.39), which is normalized by the experimental value of a neutron lifetime, $\tau_n \simeq 886.7$ s. In the nondegeneracy limit ($\mu_e \ll k_B T$), it is easily estimated by

$$\dot{q}_{Ne} = 9.2 \times 10^{33} \text{ ergs cm}^{-3} \text{ s}^{-1} \left(\frac{T}{10^{11} \text{ K}}\right)^6 \left(\frac{\rho}{10^{10} \text{ g cm}^{-3}}\right). \tag{45}$$

On the other hand, it is a little complicated to estimate the electron capture rate in the electron-degeneracy regime. In the electron-degeneracy only regime, we have

$$\dot{q}_{Ne} = 1.1 \times 10^{31} \eta_e^9 \text{ ergs cm}^{-3} \text{ s}^{-1} \left(\frac{T}{10^{11} \text{ K}}\right)^9 \tag{46}$$

for the complete-degeneracy limit of electrons. Note that in this limit, we can also independently obtain the chemical potential of electrons by the balance between the two dominant weak interaction rates, i.e., $\dot{q}_{p+e^- \to n+\nu_e} = 5.3 \times 10^{30} \eta_e^9$ ergs cm^{-3} s^{-1} $(T/10^{11}$ K$)^9$ and $\dot{q}_{n+e^+ \to p+\bar{\nu}_e} = 2.6 \times 10^{37} \exp[-m_e/(k_B T)] \exp(-\eta_e)$ ergs cm^{-3} s^{-1} $(\rho/10^{13}$ g cm$^{-3})(T/10^{11}$ K$)^6$. Compared with the chemical potential obtained in equation (26), where we assumed complete β-equilibrium, they agree with each other to within just a few percent, e.g., $\eta_e \simeq 3.5$ at $\rho = 10^{13}$ g cm^{-3} and $T = 10$ MeV/k_B. Therefore, our assumptions of the complete-degeneracy limits should be reasonable.

When both electrons and nucleons are degenerate, the reactions $p + e^- \leftrightarrow n + \nu_e$ are suppressed by Fermi blocking of degenerate nucleons in the final states. Then, for example, the dE_e integration in equation (43) is limited as $[\mu_e, \infty]$, and we approximately obtain the relatively small cooling rate, $\dot{q}_{Ne} = 5.0 \times 10^{32} \eta_e^7$ ergs cm^{-3} s$^{-1}(T/10^{11}$ K$)^9$. Compared with equation (46), of course, we find that this rate is smaller by a factor of $1/\eta_e^2$ in the complete-degeneracy regime, i.e., $\eta_e \gg 1$.

The electron-positron pair annihilation rate through $e^+ + e^- \to \nu + \bar{\nu}$ is

$$\dot{q}_{e^+ e^-} = 4.8 \times 10^{33} \text{ ergs cm}^{-3} \text{ s}^{-1} \left(\frac{T}{10^{11} \text{ K}}\right)^9 \tag{47}$$

in the nondegeneracy regime (see, e.g., Itoh et al. 1989). When the electrons are degenerate, the electron-positron pair annihilation rate is too small to compete with the other cooling process, and we can neglect it.

The nucleon-nucleon bremsstrahlung rate through $n + n \to n + n + \nu + \bar{\nu}$ is represented by

$$\dot{q}_{\text{brems}} = 3.4 \times 10^{33} \text{ ergs cm}^{-3} \text{ s}^{-1} \left(\frac{T}{10^{11} \text{ K}}\right)^8$$
$$\times \left(\frac{\rho}{10^{13} \text{ g cm}^{-3}}\right)^{1/3} \tag{48}$$

in the degeneracy regime of nucleons (Hannestad & Raffelt 1998), and

$$\dot{q}_{\text{brems}} = 1.5 \times 10^{33} \text{ ergs cm}^{-3} \text{ s}^{-1} \left(\frac{T}{10^{11} \text{ K}}\right)^{5.5}$$
$$\times \left(\frac{\rho}{10^{13} \text{ g cm}^{-3}}\right)^2 \tag{49}$$

in the nondegeneracy regime of nucleons (Hannestad & Raffelt 1998; Burrows et al. 2000).

It is also known that the plasmon decay is effective at high densities and in high electron degeneracy regions (Schinder et al. 1987). The decay rate of the transverse plasmons, which are normal photons interacting with the electron gas through $\tilde{\gamma} \to \nu_e + \bar{\nu}_e$, is estimated by Ruffert, Janka, & Schäfer (1996) as

$$\dot{q}_{\text{plasmon}} = 1.5 \times 10^{32} \text{ ergs cm}^{-3} \text{ s}^{-1} \left(\frac{T}{10^{11} \text{ K}}\right)^9$$
$$\times \gamma_p^6 e^{-\gamma_p} (1 + \gamma_p) \left(2 + \frac{\gamma_p^2}{1 + \gamma_p}\right), \tag{50}$$

where $\gamma_p = 5.565 \times 10^{-2} [(\pi^2 + 3\eta_e^2)/3]^{1/2}$. In particular, $\tilde{\gamma} \to \nu_e + \bar{\nu}_e$ is the dominant process by a factor of ~ 163 compared to the other flavors ($\to \nu_\mu \bar{\nu}_\mu$ or $\nu_\tau \bar{\nu}_\tau$).

Note that in NPK01 only the cases of equations (45) and (47) were considered in $\dot{q}_\nu$. To see what component of the cooling rates mainly contributes to the process, in Figure 2 we plot the most dominant one on the (Σ, T) plane. It is interesting to note that the region where advective energy transport dominates covers a rather wide, large-Σ and high-T part of the Σ-T diagram. This is because Q_{adv} ($\propto T^{16}$) has a stronger T dependence than Q_{rad} ($\propto T^4$) (shown below). Also note that neutrino cooling is essential only at very high temperatures ($T \gtrsim 10^{11}$ K) and very high matter density $\rho \gtrsim 10^{10}$–10^{13} g cm^{-3}. The striped region represents the region where heavy elements are produced, which are expected from the equation of state of nuclear matter (Shen et al. 1998; Ishizuka, Ohnishi, & Sumiyoshi 2002). Here, we adopt the case of the electron fraction $Y_e \simeq 0.1$ which the numerical simulations of coalescing neutron stars predict, e.g., see Ruffert et al. (1997). Note that the left side of the boundary of the striped region is just a virtual one; the tail realistically continues further to the left. As a result, there exist just a small number of free nucleons, and the neutrino processes that we consider in this study are no longer effective there.

Next, in Figure 3, we plot the heating and cooling rates as a function of the temperature for some representative values of surface density: $\Sigma = 10^{3.5}$ g cm^{-2} (Fig. 3a), 10^8 g cm^{-2} (Fig. 3b), and 10^{20} g cm^{-2} (Fig. 3c). In Figure 3a, we find three intersection points. They contain two points at which the energy balance is realized as a result of the radiative or advective cooling processes. For Figure 3b, there exists only one intersection point at which the energy balance is realized because of the advective cooling processes. It is interesting that in Figure 3c, a new branch of the energy balance appears at $T \gtrsim m_e c^2/k_B$, since the neutrino-cooling process becomes effective. By plotting only the values at those intersecting points on the (Σ, T) or $(\Sigma, \dot{M})$ plane for various values of Σ, we obtain a sequence of the thermal equilibrium solutions; that is the thermal equilibrium curve.

2.4. Various Timescales

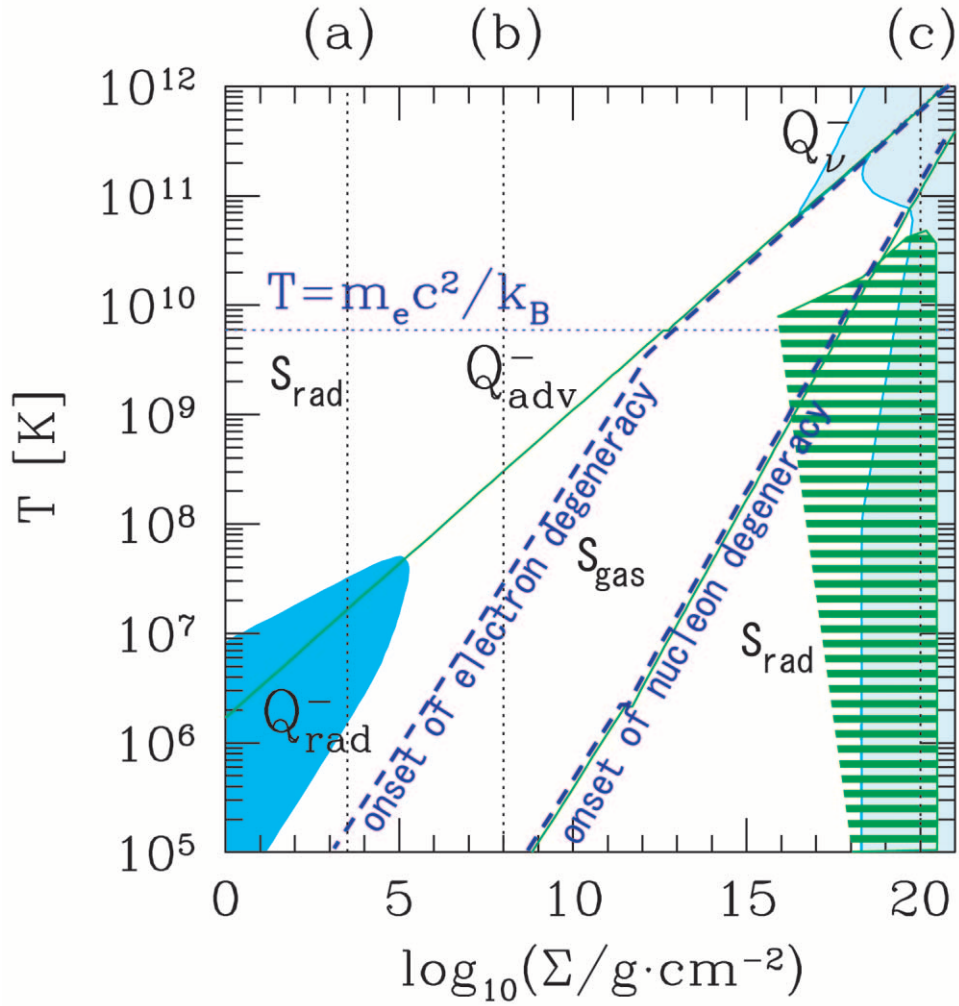Here it is necessary for us to check the timescale of the physical processes of neutrino cooling. The dynamical time-

FIG. 2.—Plot of the most dominant component in the cooling rates on the (Σ, T) plane. The adopted parameters are the viscosity parameter, $\alpha = 0.1$, the black hole mass, $M_{BH} = 3\ M_\odot$, and $r = 4r_S$. The dark shaded, light shaded, and white regions represent the places where the radiative, neutrino, and advective cooling, respectively, are the dominant processes. On the other hand, the region between the two solid lines is where the gas entropy s_{gas} mainly contributes to the total entropy. The striped region represents where heavy elements are produced, and where there exist just a small number of free nucleons. The vertical dotted lines, labelled a, b, and c, denote the representative values of Σ at which heating and cooling rates are plotted in Fig. 3. The dashed and horizontal dotted lines are the same as those in Fig. 2.
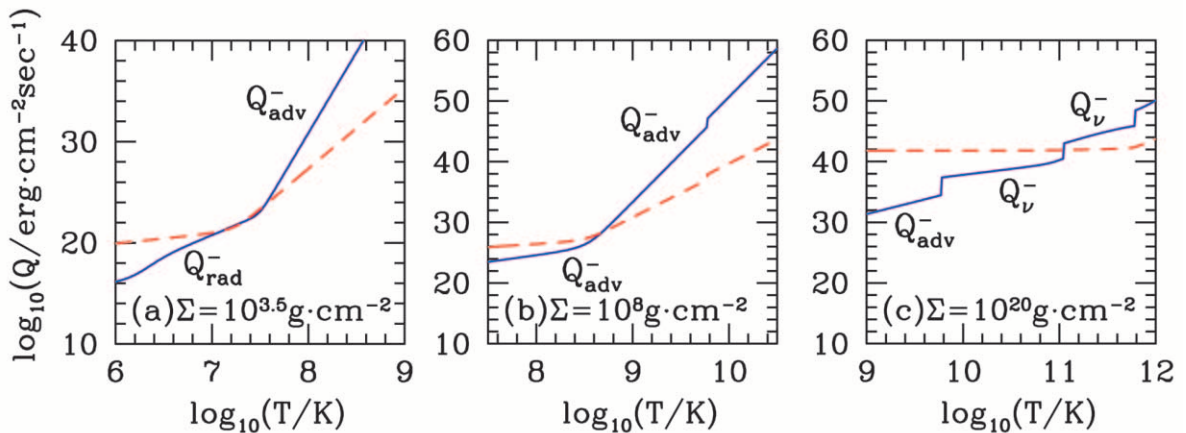

FIG. 3.—Heating and cooling rates as functions of temperature for a fixed surface density: from left to right, (a) $\Sigma = 10^{3.5}$ g cm^{-2}, (b) $\Sigma = 10^{8}$ g cm^{-2}, and (c) $\Sigma = 10^{20}$ g cm^{-2}. The other parameters are the same as in Fig. 2.

scale is represented by the accretion time,

$$\tau_{\rm acc} \equiv \frac{1}{\alpha}\sqrt{\frac{r^3}{GM_{\rm BH}}}\left(\frac{r}{H}\right)^2 \tag{51}$$

$$\simeq 1.3\times10^{-2}\ {\rm s}\ \left(\frac{\alpha}{0.1}\right)^{-1}\left(\frac{r}{4r_{\rm S}}\right)^{3/2}\left(\frac{M_{\rm BH}}{3\ M_\odot}\right), \tag{52}$$

where we assumed that the disk half-thickness is approximately $H\sim r/2$. On the other hand, the timescale of weak interaction of a nucleon off the background electrons and positrons is estimated by

$$\tau_\beta \equiv (\sigma_{Ne}n_e c)^{-1} \tag{53}$$

$$\sim 1.0\times10^{-4}\ {\rm s}\ \left(\frac{T}{10^{11}\ {\rm K}}\right)^{-5}, \tag{54}$$

where we assume that the cross section is $\sigma_{Ne}\sim G_{\rm F}^2(k_{\rm B}T)^2$, and the electron number density is $n_e\sim (k_{\rm B}T/\hbar c)^3$. Then the condition $\tau_\beta\leq\tau_{\rm acc}$ is realized when the following relation is satisfied:

$$T\geq 3.8\times10^{10}\ {\rm K}\ \left(\frac{\alpha}{0.1}\right)^{1/5}\left(\frac{r}{4r_{\rm S}}\right)^{-3/10}\left(\frac{M_{\rm BH}}{3\ M_\odot}\right)^{-1/5}. \tag{55}$$

The interaction rate of a neutrino off the background nucleons is roughly given by

$$\Gamma_{N\nu}\sim G_{\rm F}^2(k_{\rm B}T)^2 n_N c, \tag{56}$$

with the nucleon density n_N. Since $H\sim r/2$, the ratio of the interaction time $(1/\Gamma_{N\nu})$ and the neutrino crossing time (H/c) is estimated by

$$\Gamma_{N\nu}\frac{H}{c}\simeq 42.6\left(\frac{T}{10^{11}\ {\rm K}}\right)^2\left(\frac{\rho}{10^{13}\ {\rm g\ cm^{-3}}}\right)\left(\frac{r}{4r_{\rm S}}\right)\left(\frac{M_{\rm BH}}{3\ M_\odot}\right). \tag{57}$$

Since the nucleon to electron-positron ratio is $n_N/n_e\sim O(10)(\rho/10^{13}\ {\rm g\ cm^{-3}})/(T/10^{11}\ {\rm K})^{-3}$, we find that the neutrino interaction is rapid enough to realize β-equilibrium, which we have assumed in the previous subsections. When $\Gamma_{N\nu}H/c$ is greater than unity, we should modify the neutrino cooling rate in equation (41). To correctly estimate it in that case, we should divide the right-hand side of equation (41) by $\Gamma_{N\nu}H/c$. However, since the neutrino cooling rate becomes $O(10^2)$ times larger than the heating rate quite suddenly at intersection points between the cooling and the heating rates, to estimate the equilibrium curve our simple treatments in the previous section are not so wrong, and the results do not change.

Next, we estimate the vertical diffusion time of neutrinos. It is given by

$$\tau_{\rm diff}\equiv\frac{(H/c)^2}{\Gamma_{N\nu}^{-1}} \tag{58}$$

$$\simeq 2.6\times10^{-3}\ {\rm s}\ \left(\frac{T}{10^{11}\ {\rm K}}\right)^2$$

$$\times\left(\frac{\rho}{10^{13}\ {\rm g\ cm^{-3}}}\right)\left(\frac{r}{4r_{\rm S}}\right)^2\left(\frac{M_{\rm BH}}{3\ M_\odot}\right)^2. \tag{59}$$

Comparable to equation (51), the condition of $\tau_{\rm diff}\leq\tau_{\rm acc}$ is translated into

$$T\leq 2.3\times10^{11}\ {\rm K}\ \left(\frac{\alpha}{0.1}\right)^{-1/2}\left(\frac{\rho}{10^{13}\ {\rm g\ cm^{-3}}}\right)^{-1/2}$$

$$\times\left(\frac{r}{4r_{\rm S}}\right)^{-1/4}\left(\frac{M_{\rm BH}}{3\ M_\odot}\right)^{-1/2}. \tag{60}$$

Therefore, the neutrino cooling process is effective and realistic in the equilibrium solutions of the accretion disk at a high temperature, $T\sim 10^{11}$ K, and high density, $\rho\sim10^{13}$ g cm^{-3}, which will be studied in § 2.5.

2.5. Thermal Equilibrium Solutions

According to the procedure discussed in § 2.3, we can find the thermal equilibrium solutions, that is, intersecting points of the heating and cooling curves. In Figure 4 we plot them on the (Σ, T) plane for $r=4r_{\rm S}$ (left panel) and $r=40r_{\rm S}$ (right panel). In the parameter region where neutrino cooling is effective, the dominant processes are the electron capture rate ($N+e\to N'+\nu$).

Using equation (32), we can also express the mass accretion rate $\dot{M}$ at the intersection points as a function of Σ. The thermal equilibrium curves on the $(\Sigma, \dot{M})$ plane are plotted in Figure 5. Here, the mass accretion rate is normalized by the critical mass accretion rate,

$$\dot{M}_{\rm crit} = 16L_{\rm Edd}/c^2, \tag{61}$$

where $L_{\rm Edd}$ is the Eddington luminosity,

$$L_{\rm Edd} = 4\pi GM_{\rm BH}m_p c/\sigma, \tag{62}$$

with proton mass m_p and cross section σ of the matter and radiation through electromagnetic scattering, i.e., $L_{\rm Edd}/c^2\simeq 7.3\times10^{-17}\ M_\odot\ {\rm s}^{-1}(\sigma/\sigma_{\rm T})^{-1}(M_{\rm BH}/M_\odot)$, with the Thomson cross section $\sigma_{\rm T}\simeq 0.6652$ mbarn.

There are five distinct branches seen in these plots (see Table 1). In the lower left parts of both figures, the equili-

TABLE 1
T-Σ AND $\dot{M}$-Σ RELATIONS IN VARIOUS REGIMES

Regime	p	Q^+	Q^-	T-Σ relation	$\dot{M}$-Σ relation
I	$p_{\rm gas}$	$\alpha\Sigma Tr^{-3/2}M_{\rm BH}^{1/2}$	$Q_{\rm rad}^-\propto\Sigma^{-1}T^4$	$\alpha^{1/3}\Sigma^{2/3}r^{-1/2}M_{\rm BH}^{1/6}$	$\alpha^{4/3}\Sigma^{5/3}rM_{\rm BH}^{-1/3}$
II	$p_{\rm rad}$	$\alpha\Sigma^{-1}T^8r^{3/2}M_{\rm BH}^{-1/2}$	$Q_{\rm rad}^-\propto\Sigma^{-1}T^4$	$\alpha^{-1/4}\Sigma^0r^{-3/8}M_{\rm BH}^{1/8}$	$\alpha^{-1}\Sigma^{-1}r^{3/2}M_{\rm BH}^{-1/2}$
III	$p_{\rm rad}$	$\alpha\Sigma^{-1}T^8r^{3/2}M_{\rm BH}^{-1/2}$	$Q_{\rm adv}^-\propto\alpha\Sigma^{-3}T^{16}r^{11/2}M_{\rm BH}^{-5/2}$	$\alpha^0\Sigma^{1/4}r^{-1/2}M_{\rm BH}^{1/4}$	$\alpha\Sigma r^{1/2}M_{\rm BH}^{1/2}$
IV	$p_{d,{\rm rel}}$[a]	$\alpha\Sigma^{9/7}r^{-27/14}M_{\rm BH}^{9/14}$	$Q_{\rm adv}^-\propto\alpha\Sigma T^2r^{-1/2}M_{\rm BH}^{-1/2}$	$\alpha^0\Sigma^{1/7}r^{-5/7}M_{\rm BH}^{4/7}$	$\alpha\Sigma^{9/7}r^{15/14}M_{\rm BH}^{-5/14}$
V	$p_{d,{\rm rel}}$	$\alpha\Sigma^{9/7}r^{-27/14}M_{\rm BH}^{9/14}$	$Q_\nu^-\propto\eta_e^9 T^9\Sigma^{1/7}r^{9/7}M_{\rm BH}^{-3/7}$	$\Sigma^{4/7}r^{-6/7}M_{\rm BH}^{2/7}$	$\alpha\Sigma^{9/7}r^{15/14}M_{\rm BH}^{-5/14}$

[a] Here $p_{\rm gas}$ also contributes to the pressure secondly and induces the T-dependence in $Q_{\rm adv}^-$.
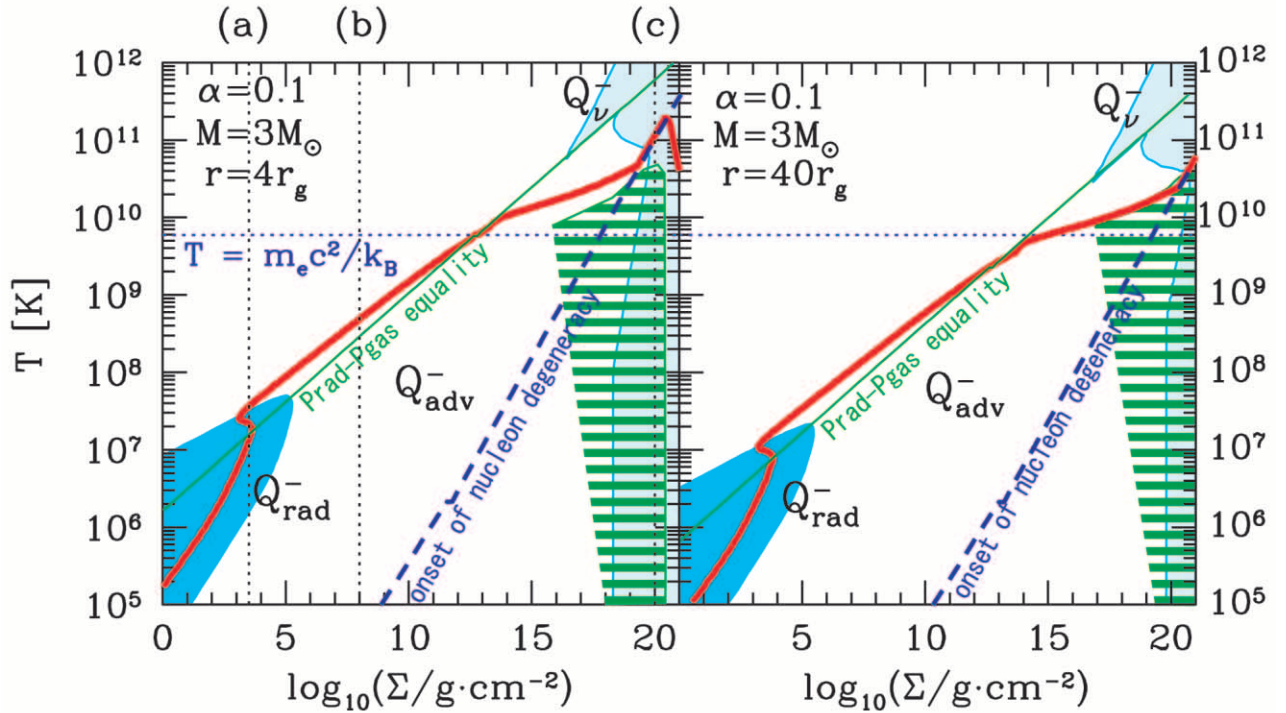
Fig. 4.—Thermal equilibrium curves (*thick solid line*) on the (Σ, T) planes at radial distances of $r = 4r_S$ (*left panel*) and $r = 40r_S$ (*right panel*). The adopted parameters are $\alpha = 0.1$ and $M_{BH} = 3\ M_\odot$. The vertical dotted lines labelled a, b, and c denote the three representative values of Σ adopted in plotting Fig. 3. The thin line indicates the loci where gas pressure equals radiation pressure. The dashed line indicates the loci where nucleon degeneracy sets out. We also indicate dominant sources of cooling by shaded zones as in Fig. 2. In the striped region, there exist just a small number of free nucleons, and neutrino cooling does not work well.

brium sequence has an S shape (see Abramowicz et al. 1988), which arises because of changes in sources of pressure (gas and radiation pressure) and in sources of cooling (radiation and advection). In the upper branch of the S shape,
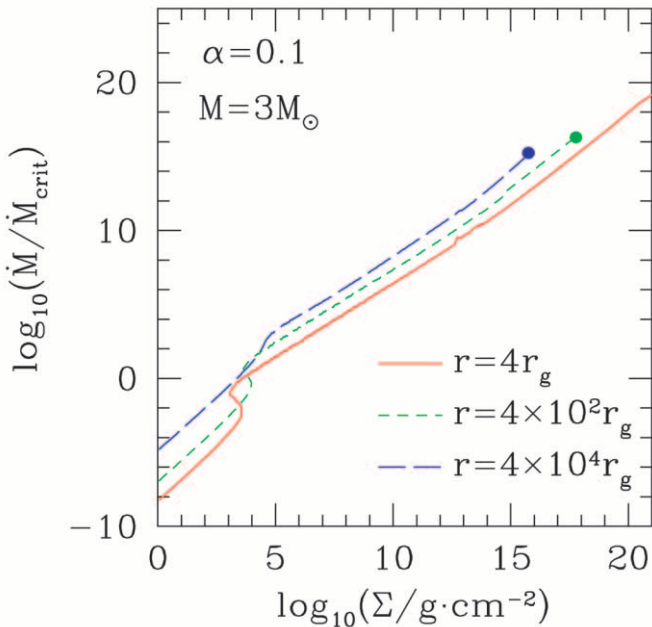

Fig. 5.—Thermal equilibrium curves on the (Σ, $\dot{M}$) plane at $r = 4r_S$ (*solid line*), $400r_S$ (*dashed line*), and $4 \times 10^4\ r_S$ (*long-dashed line*). All other parameters are the same as in Fig. 4. The solid circles at the upper ends indicate the location of $H = r$, above which no physical solution exists.

advective energy transport takes over radiative cooling. Then generated photons inside the disk take long time to escape from the disk surface, so that photons are advected inward and are finally swallowed by a central black hole with accreting matter, and disk luminosity is largely reduced. Such trapping effects should occur in branches III and IV with even higher $\dot{M}$. Neutrino cooling is dominant only in the high temperature and density regimes (branch V), in which neutrinos, instead of radiation, can carry away the generated energy inside the disk. In branch V of Table 1, we write Q_ν^- in the case where only electrons are degenerate. On the other hand, in the case where both electrons and nucleons are degenerate, Q_ν^- becomes smaller by a factor of $1/\eta_e^2$. Then the thermal equilibrium solution is only realized on the line of the condition of nucleon degeneracy. In other words, the T-Σ relation of branch V coincides with that of nucleon degeneracy. In the intermediate branch (IV) advective cooling is still dominant; however, note that entropy transported by advection is contributed by nondegenerate nucleons, since the entropy of degenerate particles is small.

It is interesting to examine the stability of each branch. The criterion for thermal instability is

$$\left(\frac{dQ^+}{dT}\right)_\Sigma > \left(\frac{dQ^-}{dT}\right)_\Sigma, \qquad (63)$$

whereas that for the viscous (secular) instability is

$$\left(\frac{d\dot{M}}{d\Sigma}\right)_{Q^+=Q^-} < 0 \qquad (64)$$

(see, e.g., Kato et al. 1998). We understand immediately

from Table 1 that only branch II (radiation pressure–dominant standard disk branch) is unstable for both modes, and all other branches, including the NDAF branch, are stable for any modes, as already noted by NPK01.

2.6. Properties of Neutrino-cooled Disks

From the equilibrium solutions found in § 2.5, we derive the following expressions for the temperature and density on the equatorial plane and for the corresponding mass accretion rates as a function of radius for a given value of Σ:

$$T = 1.1 \times 10^{11} \text{ K} \left(\frac{\Sigma}{10^{20} \text{ g cm}^{-2}}\right)^{4/7} \left(\frac{r}{4r_S}\right)^{-6/7} \left(\frac{M_{BH}}{3 \, M_\odot}\right)^{2/7},$$
(65)

$$\rho = 2.3 \times 10^{13} \text{ g cm}^{-3} \left(\frac{\Sigma}{10^{20} \text{ g cm}^{-2}}\right)^{6/7}$$
$$\times \left(\frac{r}{4r_S}\right)^{-9/7} \left(\frac{M_{BH}}{3 \, M_\odot}\right)^{3/7},$$
(66)

and

$$\dot{M} = 1.1 \times 10^{17} \dot{M}_{crit} \left(\frac{\alpha}{0.1}\right) \left(\frac{\Sigma}{10^{20} \text{ g cm}^{-2}}\right)^{9/7}$$
$$\times \left(\frac{r}{4r_S}\right)^{15/14} \left(\frac{M_{BH}}{3 \, M_\odot}\right)^{-5/14}.$$
(67)

Note that NPK01 derived similar expressions, but in terms of the disk mass, M_{disk}, and the size of the initial torus, R_{out}, which are roughly related to surface density as

$$\Sigma \approx \frac{2M_{disk}}{\pi b R_{out}^2} \sim \frac{10^{20}}{b} \text{ g cm}^{-2} \left(\frac{M_{disk}}{M_\odot}\right) \left(\frac{R_{out}}{5 \times 10^6 \text{ cm}}\right)^{-2},$$
(68)

where b is a constant of order unity, which varies depending on the geometry of the initial torus, and where we have assumed a uniform surface density distribution. We thus understand that neutrino cooling dominates only if a solar mass of material is contained within a disk of size $\sim 5 \times 10^6$ cm. In other words, if the disk mass is less or if the disk size is larger, neutrino cooling never becomes dominant. This constraint is more severe than that obtained by NPK01.

By comparing the left and right panels in Figure 4, we note that even at such a high surface density as $\Sigma \sim 10^{20}$ g cm^{-2}, the neutrino cooling does not become dominant at a somewhat larger radius (i.e., $r \gtrsim 40 r_S$). This also supports the claim by NPK01 that the NDAF solution only appears in a rather compact region around the center.

We can get a crude approximation for the strength of magnetic fields by using the above results. The equipartition field strength, for which the magnetic energy is equal to gas energy, is

$$B_{eq} = \left(\frac{8\pi \rho k_B T}{m_p}\right)^{1/2}$$
$$\simeq 7.3 \times 10^{16} \text{G} \left(\frac{\alpha}{0.1}\right)^{1/12} \left(\frac{\Sigma}{10^{20} \text{ g cm}^{-2}}\right)^{5/7}$$
$$\times \left(\frac{r}{4r_S}\right)^{-15/14} \left(\frac{M_{BH}}{3 \, M_\odot}\right)^{5/14}.$$
(69)

Therefore, the strength of the magnetic field is very likely to exceed the critical value (e.g., Mészáros 1992, p. 30),

$$B_{crit} \equiv \frac{m_e^2 c^3}{e\hbar} \simeq 4.4 \times 10^{13} \text{ G},$$
(70)

even if the fields strength is only 0.1% of the equipartition value (for which magnetic energy is only 10^{-4}% of the particle energy). It is interesting to note that the equilibrium B value is about the critical field for the proton,

$$B_{crit,p} = (m_p/m_e)B_{crit} \simeq 8 \times 10^{16} \text{ G}.$$
(71)

Then various quantum-electrodynamical (QED) effects should manifest themselves (see § 3).

3. DISCUSSION

3.1. CDAF and Slim Disk

The present study is similar to that of NPK01, although there are some differences. We newly take into account the effects of the electron and nucleon degeneracy in neutrino cooling processes. The resulting disk density and temperature differ in the neutrino-dominated regimes. In the present study we also use the slim-disk picture, instead of the CDAF picture adopted by NPK01, at moderately large Σ (and thus $\dot{M}$) ranges. As mentioned above, the properties of the hypercritical accretion flow are not yet clear, since full multidimensional simulations coupled with radiation hydrodynamics (RHD) and possibly with magnetohydrodynamics (MHD) are necessary to settle this issue. Probably convection plays a key role (Agol et al. 2001), but RHD simulations made so far in the hypercritical regimes are based on the approximation of the flux-limited diffusion (e.g., Eggum, Coroniti, & Katz 1988; Fujita & Okuda 1998), which may not hold within highly turbulent media. Also, magnetic reconnection, which is not easy to simulate in realistic situations with extremely high magnetic Reynolds number, seems to play an important role (see below).

Our conclusion basically agrees with that of NPK01 in that NDAF appears at small radii only for high M_{disk}/r_{out}^3 cases. NPK01 concluded that models involving the mergers of BH-NS binaries and of NS-NS binaries are favored to explain short GRBs because then the flow is likely to be NDAF. However, the condition we found for the NDAF is more stringent than that they found and may not be generally satisfied.

NPK01 also argue that the mergers of BH-WD binaries and BH–helium star binaries are difficult to use to explain GRBs, for the following reason. Such mergers will create disks with large dimensions, thus being unable to reach NDAF regimes but leading to the formation of CDAF. Then convective motion mostly transports energy outward, liberating little energy at small radii. These disks are thus unlikely to cause violent explosions such as GRBs. However, we would like to point out that the flow pattern is rather uncertain in the presence of magnetic fields.

If there are strong magnetic fields with poloidal (vertical) components, for example, the formation of outflows (or jets) is unavoidable (e.g., Blandford & Payne 1982; Kudoh, Matsumoto, & Shibata 1998), and such outflowing matter can produce enormous amounts of synchrotron photons. Magnetic reconnections, giving rise to intense flare emission, may also occur. In other words, mergers of BH and

WD or helium stars cannot be rejected as possible origins of GRBs. More careful discussion is needed regarding this issue.

3.2. Proof of $p_{rad} > p_{gas}$ in Electron Nondegeneracy

There are some discrepancies between the results of the present study and those of NPK01. These mainly arise from a difference in the method. NPK01, for example, analytically studied the scaling law of physical parameters in NDAF in two regimes, i.e., (1) the gas pressure–dominated regime, and (2) the degeneracy pressure–dominated regime. Here we show that gas pressure never becomes dominant whenever electrons are not degenerate at $T \gtrsim m_e c^2 / k_B$. Namely, only when electrons are degenerate can either gas pressure or degeneracy pressure become dominant, i.e., case 1 is not realized in electron nondegeneracy.

Using equations (6) and (7) with the condition $n_p \sim n_n$, we obtain the relation

$$\frac{p_{rad}}{p_{gas}} \simeq 13.02 \left(\frac{\rho}{10^7 \text{ g cm}^{-3}} \right)^{-1} \left(\frac{T}{\text{MeV}} \right)^3 . \quad (72)$$

On the other hand, the nondegeneracy condition for relativistic electrons (see eq. [12]) is represented by

$$\left(\frac{\rho}{10^7 \text{ g cm}^{-3}} \right)^{-1} \left(\frac{T}{\text{MeV}} \right)^3 \gg 0.1142 . \quad (73)$$

From equations (72) and (73), we see that the relation

$$p_{rad} \gg p_{gas} \quad (74)$$

is always realized in the nondegenerate electron regime at $T \gtrsim m_e c^2 / k_B$.

3.3. Expected QED Effects Arising from Supercritical Magnetic Fields

When the field strength exceeds the critical value [$\gtrsim O(10^{13})$ G], QED processes become important. Then, as it were, magnetic fields themselves behave as ''particles'' in the strongly magnetized vacuum, thus producing several unique features. For example, strong magnetic fields induce large energy splitting of Landau levels, large refractive indices of photons, photon-splitting effects, and so on (see, e.g., Adler 1971; Shabad 1975; Melrose & Stoneham 1976; Chistyakov, Kuznetsov, & Mikheev 1998; Kohri & Yamada 2002). In particular, the photon-splitting effect is interesting when we consider the present model of a hypercritical accretion disk to a central engine of GRBs. This is because if the rate of photon splitting ($\gamma \rightarrow 2\gamma$) is larger than that of $e^{\pm}$ pair production ($\gamma + \gamma \rightarrow e^+ + e^-$), high-energy photons with energy $E_\gamma \gg$ MeV can lose kinetic energy rapidly and produce a lot of soft photons ($E_\gamma \lesssim 0.511$ MeV) without producing copious electron-positron pairs. Then it may be possible to produce a fireball as a source of GRBs without requiring a large Lorentz factor.

Unfortunately, however, concrete values of the photon-splitting rate near the threshold energy of pair production have not been calculated precisely except for some formal formulations (Adler 1971; Shabad 1975; Melrose & Stoneham 1976). A numerical study above the threshold is currently underway (K. Kohri & S. Yamada 2002, in preparation) and needs further attention.

In addition, radiative processes in an ultramagnetized plasma are inherently complicated, and we are still far from having the basic physics under control. At the enormous densities we are dealing with, the optical depth is huge, so radiative transfer must be solved. Therefore, the above predictions may be premature at present. Only a detailed radiative transfer calculation, which is outside the present capabilities of numerical codes, could address this point.

3.4. Detectability of Neutrinos from NDAFs

As we have shown in the previous sections, we expect that a lot of neutrinos would be emitted from NDAF. It is thus of great importance to check whether the signals of the neutrinos are detectable or not in GRB events. Moreover, it is also informative to find some correlations between neutrino emission and photon emission from GRBs in terms of the observed times and/or directions to the source of the neutrinos.

Such an investigation has already been initiated by Nagataki & Kohri (2001), who computed the neutrino luminosity and its detectability, properly considering the time evolution of the central BH. Their calculations are based not on the merger models but on the collapsar model, and they adopt the simple analytical fitting formula to the hypercritical (slim) disk model taken from Fujimoto et al. (2001). (The basic numbers are in good agreement with those obtained by the numerical evaluations by Popham et al. 1999.) Their conclusion is that we will be able to marginally detect the neutrinos from collapsars occurring with TITAND, a next-generation multi-megaton water Cerenkov detector (Suzuki 2001). The first phase of TITAND is planned to have 2 Mton of water inside. We will also be able to know the direction to the source of neutrinos in TITAND. For the total number of emitted $\overline{\nu}_e$, we roughly evaluate

$$N_{\overline{\nu}_e} \sim \frac{\dot{q}_{Ne} V \Delta t}{\overline{E}_{\overline{\nu}_e}} \quad (75)$$

$$\sim 10^{57} \left(\frac{\dot{q}_{Ne}}{10^{35} \text{ ergs cm}^{-3} \text{ s}^{-1}} \right) \left(\frac{\overline{E}_{\overline{\nu}_e}}{10 \text{ MeV}} \right)^{-1}$$

$$\times \left(\frac{V}{10^{20} \text{ cm}^3} \right) \left(\frac{\Delta t}{10^{-3} \text{ s}} \right) , \quad (76)$$

with their mean energy $\overline{E}_{\overline{\nu}_e}$ to be emitted during one GRB event, where $\dot{q}_{Ne}$ is estimated at $T \simeq 10$ MeV$/k_B$ and $\rho = 10^{13}$ g cm^{-3}, V is the volume of the emitting region, and Δt is the duration. For the event number of $\overline{\nu}_e$'s,

$$R_{event} \sim 10 \left(\frac{d}{3 \text{ Mpc}} \right)^{-2} \left(\frac{N_{\overline{\nu}_e}}{10^{57}} \right) \left(\frac{\overline{E}_{\overline{\nu}_e}}{10 \text{ MeV}} \right)^2 \left(\frac{V_{H_2O}}{2 \text{ Mton}} \right) \quad (77)$$

will be detected by TITAND, where d is the distance from the source and V_{H_2O} is the volume of water. Hence, we optimistically expect to detect neutrinos from NDAFs, if the GRB occurs within a distance of 3 Mpc. If detected, neutrino signals and correlations with the GRB will be able to make clear the unknown explosion mechanism of GRBs. In order to derive reliable estimations of neutrino flux, however, we should perform detailed computations, as was done by Nagataki & Kohri (2001). This is left as future work.

4. CONCLUSION

We study the properties of hypercritical accretion flow for surface density exceeding about 10^{20} g cm^{-2}, which is realized when about a solar mass of material is contained within a disk of size $\sim 5 \times 10^6$ cm. We find the following unique features:

1. The radiation luminosity of such a flow is practically zero because of significant photon trapping, although the mass accretion rate enormously exceeds the critical rate, $\dot{M} \gg L_{\mathrm{Edd}}/c^2$.

2. Neutrino cooling dominates over advective cooling. Thus, the flow can cool via neutrino emission. We expect to detect neutrinos from GRBs with the next-generation, multi-megaton water Cerenkov detector in future.

3. Electron degeneracy pressure dominates over gas and radiation pressure, and degenerate electrons definitely influence the processes of neutrino emission. This feature is distinct from that of the solution found by NPK01.

4. The disks are stable against both thermal and viscous instabilities, even when we take electron degeneracy into account.

5. Magnetic field strength exceeds the critical value, even if we take only 0.1% of the equipartition value. Then photon splitting may occur, producing a significant number of photons of energy below ~ 511 keV, thereby possibly suppressing $e^{\pm}$ pair creation. However, quantitative discussion is left to a future work.

REFERENCES

Abramowicz, M. A., Czerny, B., Lasota, J. P., & Szuszkiewicz, E. 1988, ApJ, 332, 646
Adler, S. L. 1971, Ann. Phys., 67, 599
Agol, E., Krolik, J., Turner, N.J., & Stone, J. M. 2001, ApJ, 558, 543
Blandford, R. D., & Payne, D. G. 1982, MNRAS, 199, 883
Burrows, A., Young, T., Pinto, P., Eastman, R., & Thompson, T. A. 2000, ApJ, 539, 865
Chevalier, R. 1996, ApJ, 459, 322
Chistyakov, M. V., Kuznetsov, A. V., & Mikheev, N. V. 1998, Phys. Lett. B, 434, 67
Eichler, D., Livio, M., Piran, T., & Schramm, D. N. 1989, Nature, 340, 126
Eggum, G. E., Coroniti, F. V., & Katz, J. I. 1988, ApJ, 330, 142
Fryer, C. L., Woosley, S. E., Herant, M., & Daview, M. B. 1999, ApJ, 520, 650
Fujimoto, S., Arai, K., Matsuba, R., Hashimoto, M., Koike, O., & Mineshige, S. 2001, PASJ, 53, 509
Fujita, M., & Okuda, T. 1998, PASJ, 50, 639
Goodman, J. 1986, ApJ, 308, L47
Hannestad, S., & Raffelt, G. 1998, ApJ, 507, 339
Igumenshchev, I. V., Abramowicz, M. A., & Narayan, R. 2000, ApJ, 537, L27
Ishizuka, C., Ohnishi, A., & Sumiyoshi, K. 2002, preprint (nucl-th/0201026)
Itoh, N., Adachi, T., Nakagawa, M., Kohyama, Y., & Munakata, H. 1989, ApJ, 339, 354 (erratum 360, 741 [1990])
Kato, S., Fukue, J., & Mineshige, S. 1998, Black Hole Accretion Disks (Kyoto: Kyoto Univ. Press)
Kohri, K., & Yamada, S. 2002, Phys. Rev. D, 65, 043006
Kudoh, T., Matsumoto, R., & Shibata, K. 1998, ApJ, 508, 186
MacFadyen, A. I., & Woosley, S. W. 1999, ApJ, 524, 262
Melrose, D. B., & Stoneham, R. J. 1976, Nuovo Cimento, 32, 435
Mészáros, P. 1992, High-Energy Radiation from Magnetized Neutron Stars (Chicago: Univ. Chicago Press)
Mészáros, P. 2001, Science, 291, 79
Mészáros, P., Rees, M. J., & Wijers, R. 1999, NewA, 4, 303
Nagataki, S., & Kohri, K. 2001, Prog. Theor. Phys., submitted
Narayan, R., Igumenshchev, I. V., & Abramowicz, M. A. 2000, ApJ, 539, 798
Narayan, R., Paczyński B., & Piran T. 1992, ApJ, 395, L83
Narayan, R., Piran T., & Kumar P. 2001, ApJ, 557, 949 (NPK01)
Paczyński, B. 1986, ApJ, 308, L43
———. 1991, Acta Astron., 41, 257
———. 1998, ApJ, 494, L45
Piran, T. 2000, Phys. Rep., 333, 529
Popham, R., Woosley, S. E., & Fryer, C. 1999, ApJ, 518, 356
Quataert, E., & Gruzinov, A. 2000, ApJ, 539, 809
Rees, M. J., & Mészáros, P. 1992, MNRAS, 258, P41
———. 1994, ApJ, 430, L93
Ruffert, M., & Janka, H.-Th. 1999, A&A, 344, 573
Ruffert, M., Janka, H.-Th., & Schäfer, G. 1996, A&A, 311, 532
Ruffert, M., Janka, H.-Th., Takahashi, K., & Schäfer, G. 1997, A&A, 319, 122
Shabad, A. E. 1975, Ann. Phys., 90, 1975
Shen, H., Toki, H., Oyamatsu, K., & Sumiyoshi, K. 1998, Prog. Theor. Phys., 100, 1013
Shinder, P. J., Schramm, D. N., Wiita, P. J., Margolis, S. H., & Tubbs, D. L. 1987, ApJ, 313, 531
Spruit, H. C. 1999, A&A, 341, L1
Suzuki, Y. 2001, preprint (hep-ex/0110005)
Thompson, C. 1994, MNRAS, 270, 480
Usov, V. V. 1992, Nature, 357, 472
———. 1994, MNRAS, 267, 1035
Wijers, R., & Galama, T. 1999, ApJ, 523, 177
Woosley, S. E. 1993, ApJ, 405, 273